Topological Valley Hall Edge State Lasing

Hua Zhong, Yongdong Li, Daohong Song, Yaroslav V. Kartashov, Yiqi Zhang, Yanpeng Zhang, and Zhigang Chen*

Topological lasers based on topologically protected edge states exhibit unique features and enhanced robustness of operation in comparison with conventional lasers, even in the presence of disorder, edge deformation, or local defects. Here a new class of topological lasers arising from the valley Hall edge states is proposed, which does not rely on magnetic fields. Specifically, topological lasing occurs at domain walls between two honeycomb waveguide arrays with broken spatial inversion symmetry. Two types of valley Hall edge lasing modes are found by shaping the gain landscape along the domain walls. In the presence of uniform losses and two-photon absorption, the lasing results in the formation of stable nonlinear dissipative excitations localized on the edge of the structure, even if it has complex geometry and even if it is finite. Robustness of lasing edge states is demonstrated in both periodic and finite structures, where such states can circumvent certain corners without scattering losses or radiation into the bulk, as long as the intervalley scattering is absent. The photonic structure and mechanism proposed here for topological lasing is fundamentally different from those previously employed in topological lasers, and can be used for fabrication of practical topological lasers of various geometries.

1. Introduction

Nowadays, topological photonics [1,2] is one of the fascinating frontiers of research driven by the topology-related concepts originating from condensed matter physics.[3,4] It has attracted worldwide attention due to the unprecedented potential that topological systems bring about for manipulation of light propagation. In a photonic topological insulator, for instance, topologically protected edge states emerge as robust localized states on the edge of a bulk photonic material, immune to defects and disorder upon their evolution. Various photonic topological insulators and topologically protected edge states were realized either by breaking time-reversal symmetry with applied magnetic fields, or by implementing photonic spin–orbit interaction, or spatial inversion symmetry breaking.[5–21]

Among numerous optical structures, the photonic honeycomb lattice–also called "photonic graphene"[22]–offers a convenient platform for exploration of various topological phenomena. The spectrum of such lattices contains three pairs of degenerate but inequivalent Dirac points (**K** and **K**′) at the corners of the first Brillouin zone, as has been employed for demonstration of valley pseudospin and valley Landau–Zener–Bloch oscillations.[23,24] If two sublattices of a honeycomb lattice have different refractive indices or different sizes, the inversion symmetry will be broken and a gap will open at the Dirac points, resulting in a host of fundamental new phenomena due to the intriguing valley degree of freedom.[25,26] For instance, the Berry curvature has opposite signs at the **K** and **K**′ valleys, that can be attributed to an effective magnetic field leading to the well-known valley Hall effect.[27] It has been proven both theoretically and experimentally that, at the domain walls between two honeycomb lattices with inversion-symmetry breaking,[28,29] there exist robust topologically protected valley Hall edge states (VHESs) that can circumvent sharp corners without radiation into the bulk. Inspired by the discoveries in topological electronic systems, a variety of valley-mediated effects have been investigated on photonic platforms.[19–21,24,29–33]

So far, rich physical phenomena stemming from valley degree of freedom and the VHESs have been considered mostly in conservative systems, leaving their dissipative counterparts largely

H. Zhong, Prof. Y. D. Li, Dr. Y. Q. Zhang, Prof. Y. P. Zhang
Key Laboratory for Physical Electronics and Devices of the Ministry of Education & Shaanxi Key Lab of Information Photonic Technique
Xi'an Jiaotong University
Xi'an 710049, China
E-mail: zhangyiqi@mail.xjtu.edu.cn

H. Zhong, Dr. Y. Q. Zhang
Guangdong Xi'an Jiaotong University Academy
Foshan 528300, China

Prof. D. Song, Prof. Z. Chen
MOE Key Laboratory of Weak-Light Nonlinear Photonics
TEDA Applied Physics Institute and School of Physics
Nankai University
Tianjin 300457, China

Prof. Y. V. Kartashov
Institute of Spectroscopy
Russian Academy of Sciences
Troitsk, Moscow Region 108840, Russia

Prof. Z. Chen
Department of Physics and Astronomy
San Francisco State University
San Francisco, CA 94132, USA

The ORCID identification number(s) for the author(s) of this article can be found under https://doi.org/10.1002/lpor.202000001

DOI: 10.1002/lpor.202000001

unexplored. On the other hand, one of the most spectacular recent advances in the field of topological photonics and its technological application is the realization of topological lasers,[34–39] which are essentially dissipative systems. In such laser systems, lasing occurs based on topologically protected edge states and therefore exhibits new features outperforming conventional lasers whose stability may be affected by perturbations such as defects and disorder. In addition to lasing based on edge states in a one-dimensional (1D) Su-Schrieffer–Heeger chain,[34–37] 2D topological lasing has been achieved in photonic crystals [40] and lattices of coupled-ring resonators,[41,42] and has been proposed theoretically for Floquet topological insulators, [43] and a bosonic Harper–Hofstadter model.[44] In polariton systems, topological lasers based on 1D and 2D microresonator arrays have been experimentally demonstrated,[17,35] and lasing based on a 2D polariton topological insulator was further studied in theory when sufficiently strong pump was provided in the system.[45] However, topological lasers based on VHESs that do not require external magnetic fields or dynamical modulations of system parameters have not been explored, to the best of our knowledge.

The aim of this work is to introduce 2D VHES lasing that can be implemented using photonic honeycomb waveguide arrays with broken spatial inversion symmetry fabricated in conventional nonlinear optical transparent materials with gain saturation. We show that topologically protected VHESs at the domain wall in this system can undergo lasing if spatially inhomogeneous gain is provided. Such topological VHES lasing does not require real or artificial magnetic fields or rely on judicious engineering of coupling between elements as that based on coupled-resonator arrays. In addition, the topological lasing proposed here is based on straight waveguide arrays, so it is more feasible for experimental realization and free from radiative losses typically present in helical waveguide arrays.

2. The Model and Spectrum of the System

The propagation dynamics of light beams in our dissipative structure supporting the VHESs can be described by the nonlinear Schrödinger-like equation that in dimensionless units reads as

$$i\frac{\partial\psi}{\partial z} = -\frac{1}{2}\nabla^2\psi - [\mathcal{R}_{\rm re} - i\mathcal{R}_{\rm im} + i\gamma]\psi - (1+i\alpha)|\psi|^2\psi. \quad (1)$$

Here, $\psi = (\kappa^2 w^2 n_{2,\rm re}/n_{\rm re})^{1/2}E$ is the scaled field amplitude; x, y are the transverse coordinates normalized to the characteristic scale w; z is the propagation distance scaled to the diffraction length κw^2; $\kappa = 2\pi n_{\rm re}/\lambda$ is the wavenumber; $n_{\rm re}$ and $n_{\rm im}$ ($n_{\rm im} \ll n_{\rm re}$) are the real and imaginary parts of the unperturbed linear refractive index of the material, respectively; $n_{2,\rm re}$ and $n_{2,\rm im}$ are the real and imaginary parts of the nonlinear refractive index, respectively; $\gamma = \kappa^2 w^2 n_{\rm im}/n_{\rm re}$ is the coefficient of linear losses that are assumed uniform; $\alpha = n_{2,\rm im}/n_{2,\rm re}$ is the scaled coefficient characterizing nonlinear losses stemming from all sources, including intrinsic nonlinear losses of the medium and gain saturation in the first approximation. Further we consider a self-focusing cubic (Kerr) nonlinearity, typical for many solid materials, including optical fibers. We assume that the VHES laser is composed of two honeycomb arrays but with opposite inversion-symmetry-breaking (**Figure 1**a). The refractive index distribution in each array is described by the function $\mathcal{R}_{\rm re}(x,y) = \mathcal{R}^{\rm A}_{\rm re}(x,y) + \mathcal{R}^{\rm B}_{\rm re}(x,y)$, where $\mathcal{R}^{\rm A}_{\rm re}$ and $\mathcal{R}^{\rm B}_{\rm re}$ stand for two standard sublattices of the honeycomb array. Each sublattice $\mathcal{R}^{\rm A,B}_{\rm re}(x,y) = p^{\rm A,B}_{\rm re}\sum_{n,m}\mathcal{Q}(x-x_n, y-y_m)$ is composed of Gaussian waveguides $\mathcal{Q} = \exp[-(x^2+y^2)/d^2]$ with normalized depths of $p^{\rm A,B}_{\rm re} = \kappa^2 w^2 \delta n^{\rm A,B}_{\rm re}/n_{\rm re}$, where (x_n, y_m) are the coordinates of the sites of the honeycomb lattice and d the waveguide width. The separation between the waveguides in the array is denoted as b, and the period of this structure in the y-direction equals to $Y = 3b$ as shown in Figure 1b. Further we introduce detuning between two sublattices, i.e., we set $p^{A}_{re} > p^{B}_{re}$ (here we choose $p^{\rm A}_{\rm re} = 7$ and $p^{\rm B}_{\rm re} = 6$, so that every channel is a single-mode waveguide). An armchair domain wall[20,33,46–54] is created at the interface between such an array and another honeycomb array with inverted detuning $p^{\rm A}_{\rm re} < p^{\rm B}_{\rm re}$ between sublattices, as shown in Figure 1a by the dashed rectangle. Gain is only provided on the armchair domain wall, but selectively on the pairs of identical sites with either deeper or shallower potential, as shown in Figure 1b,f. The gain is also described by the function $\mathcal{R}_{\rm im}(x,y) = p_{\rm im}\sum_{q,l}\mathcal{Q}(x-x_q, y-y_l)$, where x_q, y_l are the coordinates of domain wall waveguides, and $p_{\rm im} = \kappa^2 w^2 \delta n_{\rm im}/n_{\rm re}$ is the gain amplitude ($p_{\rm im} \ll p^{\rm A,B}_{\rm re}$). For convenience, we label the gain profile in Figure 1b as type-I (gain on deeper sites), and that in Figure 1f as type-II (gain on shallower sites). In the following, we will explain why we consider these two types of gain landscapes. Actually, different types of domain walls can also be produced in honeycomb lattices, and we choose an armchair domain wall here because two kinds of edge states are supported by such a domain wall (see results in Figure 1), which can lead to lasing in edge states with different structure in the presence of properly shaped gain. In addition, such a domain wall can also result in interface modes with zero group velocity at $k = 0$.

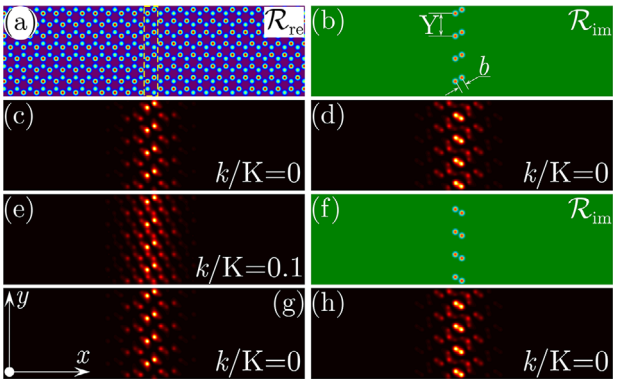

Figure 1. a) Real part of the refractive index in the array with an armchair domain wall (indicated by a dashed rectangle). b) Gain landscape of type-I with amplification on deeper sites of the armchair domain wall. c) Intensity profile of the VHES with $k = 0$ that has intensity maxima on deeper sites. d) Intensity profile of the VHES with $k = 0$ that has intensity maxima on shallower sites. e) Same as (c), but for $k = 0.1$ K. f) Gain landscape of type-II with amplification on shallower sites of the armchair domain wall and g,h) corresponding edge states of two different types. Other parameters are $d = 0.4$, $b = 1.4$, and $p_{\rm im} = 0.35$.

We would like to mention the possibility of implementation of this scheme in pumped planar periodic structures, like those used in Refs. [40,55]. In the particular case of doped chalcogenide

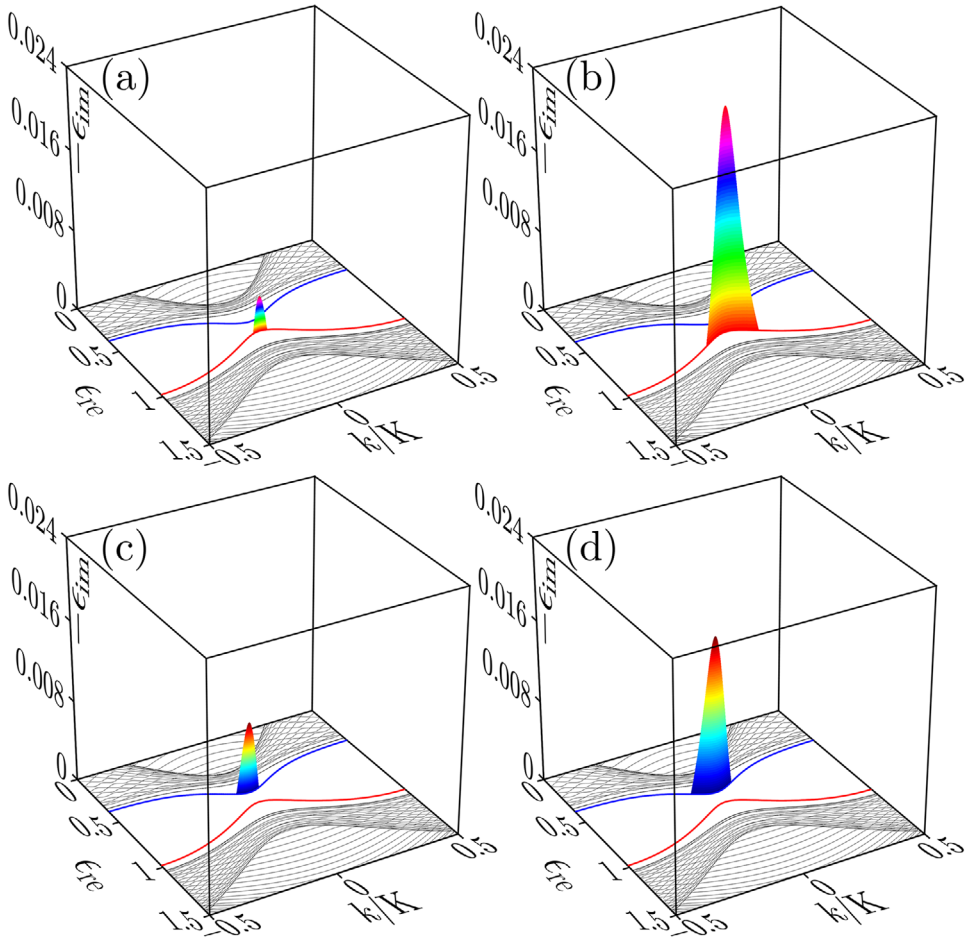

Figure 2. Real ϵ_{re} and imaginary ϵ_{im} parts of energy of the linear VHESs. (Top) Type-I gain landscape on the armchair domain wall, a) $p_{im} = 0.3$ and b) $p_{im} = 0.4$. (Bottom) Type-II gain landscape, c) $p_{im} = 0.35$ and d) $p_{im} = 0.4$. Only states with $-\epsilon_{im} > 0$ can lase, while all other states are attenuated.

glasses (such as GaLaS or AsEe with nonlinear coefficient $n_{2,re} \approx 1 \times 10^{-17}$ m^2 W^{-1} and absorption coefficient ranging from $n_{2,im} \approx 2 \times 10^{-19}$ m^2 W^{-1} to $n_{2,im} \approx 1 \times 10^{-17}$ m^2 W^{-1} depending on composition[56–58]), one finds that the dimensionless diffraction length is ~1.5 mm; the refractive index modulation depth of $p_{re}^{A,B} = 6$ corresponds to a real refractive index modulation depth $\sim 6.8 \times 10^{-4}$; while parameter $p_{im} = 0.1$ corresponds to $\delta n_{im} \approx 1 \times 10^{-5}$, for the characteristic transverse scale of $w \approx 10\,\mu$m and unperturbed refractive index $n_{re} \approx 2.81$ at the wavelength of $\lambda = 1.08\,\mu$m. The lasing proposed here does not contain a cavity and therefore it operates in a single-passage configuration. However, the governing Equation (1) can be adopted for different cavity-based structures, such as the polariton micropillar arrays under incoherent pump,[17,35] with one crucial difference that the system considered here has a focusing nonlinearity while the nonlinearity in polaritonic systems is predominantly repulsive. The other relevant example is the cavities based on structured photonic crystals, like those used in Refs. [59,60].

As a first step, we consider linear modes of our structure by setting $\alpha = 0$ and neglecting the focusing nonlinearity, but keeping the linear loss $\gamma = 0.05$ and inhomogeneous gain $\mathcal{R}_{im}$. We seek for the eigenmodes of the form $\psi(x, y, z) = u(x, y) \exp(i\epsilon z + iky)$ in the corresponding linear equation, where $u(x, y) = u(x, y + \mathrm{Y})$, k is the Bloch momentum along the y direction, and $\epsilon = \epsilon_{re} + i\epsilon_{im}$ is the propagation constant (or "energy") with ϵ_{re} and ϵ_{im} being the real and imaginary parts, respectively. The sign of the imaginary part ϵ_{im} is determined by the loss γ and gain $\mathcal{R}_{im}$. If $\epsilon_{im} < 0$, the modes are amplified, while the modes are damped if $\epsilon_{im} > 0$. **Figure 2** shows ϵ_{re} and ϵ_{im} versus normalized Bloch momentum k/K with K $= 2\pi$/Y for different gain amplitudes p_{im}. In the bandgap, there are two VHESs throughout the first Brillouin zone, which are indicated by the red and blue colors. The red edge state is concentrated mainly on deeper sites of the domain wall (Figure 1c), while blue edge state resides mainly on shallower sites (Figure 1d). This opens up unique opportunity to selectively amplify necessary state by providing gain on either deeper or shallower sites (since overall amplification exhibited by the edge state is determined by the overlap integral of its profile and gain landscape) - the reason why we introduced type-I and type-II gain landscapes. In Figure 2a,b linear band structures are plotted for the type-I gain landscape with $p_{im} = 0.3$ and $p_{im} = 0.4$. One can see that the imaginary part of the energy may assume negative values on edge state branches around $k = 0$ (in the figure we plot the inverted value $-\epsilon_{im}$ for illustrative purposes without showing the $-\epsilon_{im} < 0$ region corresponding to damped modes, hence color spikes in Figure 2 directly

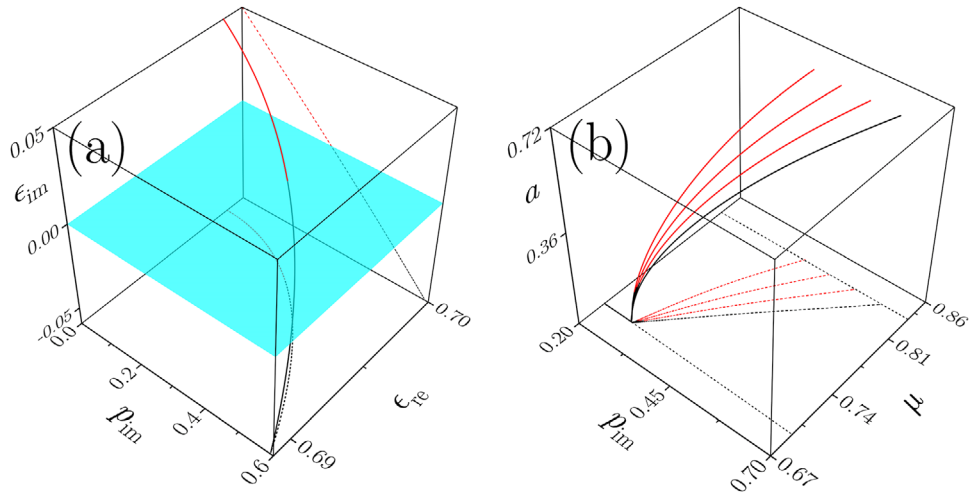

Figure 3. a) Real ϵ_{re} and imaginary ϵ_{im} parts of energy of the linear edge state with $k = 0$ versus p_{im}. Around $p_{im} \approx 0.282$, when the curve crosses blue plane, lasing in VHES occurs. b) Amplitude a and nonlinear energy shift μ of the edge state with $k = 0$ versus p_{im} for different nonlinear absorption coefficients increasing from $\alpha = 0.2$ to $\alpha = 0.5$ in steps of 0.1. Lower dashed line in (p_{im}, μ) plane indicates the energy of the linear edge state; upper dashed line is the boundary of the bandgap (viz. bottom of bulk band). Stable branches are shown black and unstable branches are shown red.

show which modes will grow upon evolution). Numerical simulations demonstrate that this happens if gain amplitude p_{im} exceeds a threshold $p_{im}^{th} \approx 0.282$, defining the threshold for lasing in VHESs. Comparing Figure 2a,b, we find that the Bloch momentum interval centered on $k = 0$, where edge states are amplified, expands with increasing gain amplitude p_{im}. For large gain levels p_{im}, lasing occurs in the entire first Brillouin zone for red edge state (that always features largest effective gain for type-I landscape), and even for bulk and blue edge states. We display red edge states obtained at $p_{im} = 0.35$ at different momenta in Figure 1c,e, while blue edge state at $k = 0$ is shown in Figure 1d. The red state in Figure 1c is amplified, but blue state in Figure 1d is damped. If the momentum of the red edge state is located out of the range, where $-\epsilon_{im} > 0$, this state is damped as well. An example is shown in Figure 1e that is out of the lasing range $-0.065\text{K} \le k \le 0.065\text{K}$ for $p_{im} = 0.35$. This picture inverts for the type-II gain profile, see corresponding band structures in Figure 2c,d. One finds that the lasing threshold for the blue edge state is about $p_{im}^{th} \approx 0.308$, which is higher than lasing threshold $p_{im}^{th} \approx 0.282$ for the red edge state. The red and blue VHESs at $k = 0$ obtained for type-II gain landscape for parameters of Figure 2c are displayed in Figure 1g,h, respectively, but this time the former state is attenuated and the latter one is amplified. Providing gain on both deep and shallow sites of the armchair domain wall may lead to simultaneous lasing in red and blue edge states, but this will lead to beatings that should be avoided if single spatial-mode operation is desired. In what follows, without loss of generality, we will consider type-I gain landscape, unless stated otherwise.

3. Valley Hall Lasing States

Amplification of the edge states at $p_{im} > p_{im}^{th}$ [see corresponding dependence of the imaginary and real parts of the energy of the amplified edge state at $k = 0$ on p_{im} illustrated in **Figure 3**a, where lasing domain associated with $-\epsilon_{im} > 0$ lies below the blue plane in the figure] can be eventually arrested by the nonlinear absorption. To explore the possibility of the exact and stable balance between diffraction, nonlinearity, gain and absorption in this system we now consider model (1) with all nonlinear terms included and search for stationary nonlinear edge states with constant power along propagation distance. Since several VHESs may experience amplification above the lasing threshold, we use linear mode of the conservative system with particular k value as an input for nonlinear Equation (1) and solve it up to sufficiently large distance. In subsequent evolution, the nonlinear competition between modes typically results in the emergence of a stationary nonlinear dissipative edge state that we further use as an input to build the entire family of dissipative solutions parameterized by gain amplitude p_{im}. The obtained solutions at selected value of the momentum k were additionally checked by the Newton method complemented by the power balance condition.

It should be stressed that we do not consider in this system spectrally limited gain profiles and temporal effects for which particular material dispersion would be relevant. Shallow waveguides used here have refractive index contrast of the order of 10^{-4} (imaginary part of the refractive index is even smaller) perfectly justifying utilization of the paraxial approximation at a single frequency. Thus, if a stable lasing edge mode emerges due to nonlinear competition between all allowed modes of the system (notice that according to Figure 2 several modes may simultaneously exhibit amplification), one can claim single spatial-mode lasing. This statement refers exclusively to spatial distributions of the lasing modes as it assumes that only one spatial mode is excited with well-defined in-gap energy and there are no other spatial modes with energies that would cause beatings in z. This regime is only possible due to nonlinear competition between different spatial modes in inhomogeneous gain landscape. Thus, the presence of nonlinearity is a key aspect of this system. It is responsible (along with nonlinear losses) for considerable reshaping and competition between different spatial modes that can be simultaneously excited in the structure. It also determines the domains of stability of the nonlinear edge states. Indeed, such states are

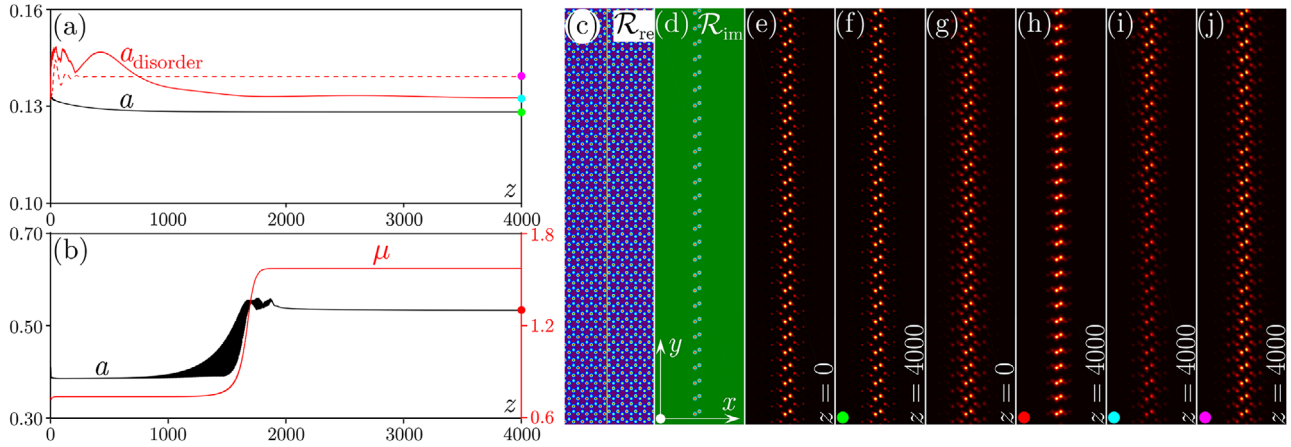

Figure 4. Peak amplitude $a = \max|\psi|$ versus distance z illustrating a) stable propagation of the lasing state at $p_{\text{im}} = 0.29$, $\alpha = 0.4$, $k = 0$ [$|\psi|^2$ distributions at $z = 0$ and $z = 4000$ are shown in e,f) – marked with green dot], and b) unstable propagation at $p_{\text{im}} = 0.36$, $\alpha = 0.4$, $k = 0$ [corresponding $|\psi|^2$ distributions at $z = 0$ and $z = 4000$ are shown in g,h) – marked with red dot]. Red curve in b) shows instantaneous value of energy μ of the unstable state versus distance z. c) Refractive index distribution with a domain wall indicated by a yellow line. d) Type-I gain profile. In addition, in a) the red curves show peak amplitudes versus z for the lasing state propagating in the lattice with diagonal small-scale (solid curve) and large-scale (dashed curve) disorder at $p_{\text{im}} = 0.29$, $\alpha = 0.4$, $k = 0$ [corresponding $|\psi|^2$ distributions at $z = 4000$ are depicted in i,j) – marked with blue and pink dots, respectively].

extended for the case of straight interface and may be affected by modulational instabilities, as discussed below.

To characterize nonlinear families of the VHESs in our lasing system, we determine their peak amplitude $a = \max|\psi|$ and the nonlinear energy shift (or propagation constant) μ as a result of Kerr nonlinearity, since in stationary states $\psi \sim \exp(i\mu z)$. Figure 3b shows the dependencies of a and μ on gain amplitude p_{im} for $k = 0$ at different values of the nonlinear absorption coefficient α. In Figure 3b the lasing threshold in p_{im} is clearly seen, where the amplitude of the lasing state becomes nonzero. Lasing in the states with nonzero momentum k can occur too, but the threshold for lasing will be higher in this case. This is because the state with $k = 0$ has largest overlap with gain landscape, leading to the most efficient amplification. Energy shift μ below the lasing threshold naturally coincides with the energy of the linear edge state (corresponding state is damped), as shown by the bottom dotted line in the (p_{im}, μ) plane in Figure 3b. Above the threshold, nonlinear energy shift increases almost linearly with gain amplitude until it reaches the bottom of the bulk band, as indicated by the upper dotted line in the (p_{im}, μ) plane in Figure 3b. Since we only consider truly localized lasing modes formed in the bandgap that do not couple to bulk modes, we show the curves only in the bandgap in Figure 3b. Topological origin of the nonlinear lasing states in this system is obvious, since by decreasing gain amplitude p_{im} one can trace back such nonlinear states exactly up to the point, where they bifurcate from linear edge modes, and where nonlinear energy shift μ exactly coincides with eigenvalue ϵ_{re} of corresponding linear mode.

By comparing the curves in Figure 3b for different nonlinear absorption coefficients, one finds that the interval of gain amplitudes where localized VHESs exist expands with the growth of the nonlinear absorption α. The regions where lasing is stable or unstable are identified in Figure 3b, where black curves correspond to stable lasing states, while red ones to unstable states (as outlined below, stability was checked by direct propagation of nonlinear lasing edge states perturbed by broadband noise). Notice that for small values of nonlinear losses α only small parts of curves close to lasing threshold are stable, while for large α values practically the entire branch becomes stable, see the curve at $\alpha = 0.5$.

The stability of these dissipative edge states is a crucial issue from the point of view of potential experimental realization. To find out the possible perturbations that could lead to instability of these states, we consider dissipative edge states on a huge transverse windows (up to 100 periods along the y axis), superimpose on them at $z = 0$ initial 5% amplitude noise, and then propagate them up to long enough distance. Exemplary stable and unstable lasing states for $k = 0$ are shown in **Figure 4** together with the array profile and gain landscape (Figure 4c,d). For illustrative purposes the intensity distributions in Figure 4 are shown only on 20 periods along y axis, while actual integration window was much larger. In Figure 4a, the peak amplitude $a = \max|\psi|$ of the perturbed VHES at $p_{\text{im}} = 0.29$ and $\alpha = 0.4$ is displayed as a function of the propagation distance. The peak amplitude quickly returns to the unperturbed value and remains unchanged up to the propagation distance $z > 4000$, demonstrating stability of the lasing state. We also show typical intensity distributions in the lasing state at $z = 0$ and $z = 4000$ (green dot in Figure 4a) in Figure 4e,f, which are almost the same except for a small difference due to the artificially introduced perturbation in Figure 4e.

In contrast, unstable evolution at $p_{\text{im}} = 0.36$ is illustrated in Figure 4b, where black curve shows $a(z)$ dependence, while instantaneous value of the energy $\mu(z)$ is shown by the red curve. Interestingly, after the transient stage $1000 < z < 2000$, where the instability develops, the wave transforms into different stable nonlinear pattern with invariable peak amplitude, see intensity distribution at $z = 4000$ in Figure 4h (corresponding to the red dot in Figure 4b). The nonlinear energy shift for this state jumps from the initial value in the gap to another value $\mu \approx 1.57$ which lies in the allowed band. This mode also has phase distribution that is substantially different from that in nonlinear state residing in the gap (neighboring spots on deep channels are not out-of-phase anymore). Penetration of μ into the band is accompanied by coupling with bulk modes, leading to small radiative

background. However, in our dissipative system this background is damped due to losses and is not visible on the scale of the figure.

We emphasize that the presence of the topological edge states at the interface is crucial for realization of stable lasing. The analysis shows (please see Section 1 in the Supporting Information) that, when interface between two lattices does not support topological edge states, the lasing threshold substantially increases up to $p_{\mathrm{im}}^{\mathrm{th}} \approx 0.55$ as compared to the threshold $p_{\mathrm{im}}^{\mathrm{th}} \approx 0.282$ in the topological system under same excitation conditions. Moreover, stable lasing cannot be achieved in the same parameter range (for the same nonlinear absorption α), where it was possible for the topological structure. The corresponding nonlinear lasing states emerging in a topological trivial system are always strongly unstable with radiation into the bulk (see Figure S1 in the Supporting Information).

Since valley scattering can take place with VHESs, it is necessary to investigate the influence of disorder on the nonlinear VHESs, even when they are dynamically stable in regular structure. To this end we first add small-scale diagonal disorder into the depths (real part only) of the individual lattice sites by taking $\mathcal{R}_{\mathrm{re}}^{\mathrm{A,B}}(x,y) = p_{\mathrm{re}}^{\mathrm{A,B}} \sum_{n,m} (1+\delta_{nm}) \mathcal{Q}(x-x_n, y-y_m)$, where δ_{nm} is a random number uniformly distributed within $[-0.02, +0.02]$. In this case nonlinear VHES remains stable and reaches steady state after certain propagation distance, as shown by the red solid curve $a_{\mathrm{disorder}}(z)$ in Figure 4a, illustrating corresponding evolution of peak amplitude of the field. However, the output intensity distribution displayed in Figure 4i clearly shows that the intervalley scattering generates backward wave, caused by small-scale disorder that has large bandwidth in the momentum space and that is capable of coupling the two valleys. The interference between the forward and backward waves results in pronounced modulation of the nonlinear edge state in the y-direction. Next, we study the dynamics of the nonlinear VHESs in a large-scale disorder introduced into the real part of the lattice as $\mathcal{R}_{\mathrm{re}}^{\mathrm{A,B}}(x,y) = \sum_{n,m} \{p_{\mathrm{re}}^{\mathrm{A,B}} + \delta[1-\cos(\omega y_m)]\} \mathcal{Q}(x-x_n, y-y_m)$ with $\delta = 0.02$ being constant and $\omega = 2\pi/(10\mathrm{Y})$. Corresponding dependence of the peak amplitude on z shown by the red dashed curve in Figure 4a and output intensity distribution in Figure 4j demonstrate that intervalley scattering disappears because large-scale disorder with small bandwidth in momentum space cannot couple two valleys and no backward wave (no modulation of the edge state) emerges. Thus, intervalley scattering of VHESs is suppressed if the bandwidth of the disorder is not sufficient to couple two valleys.

Since practical laser system should be spatially compact, here we propose the design of such spatially limited structures. Two different honeycomb lattices can be placed in contact such that domain wall exhibits relatively sharp bends allowing to create closed-contour configurations. Such structures with finite length of the edge are supposed to be beneficial for stability of edge modes, since they eliminate destructive perturbations with very large periods exceeding the length of the edge. Here,

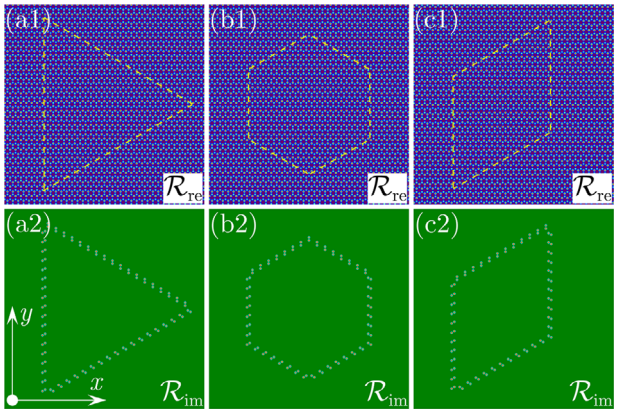

Figure 5. Design of laser systems with different geometries. a1,a2) Triangular structure. b1,b2) Hexagonal structure. c1,c2) Rhombic structure. Top row: refractive index distributions with dashed lines indicating the domain wall. Bottom row: type-I gain landscape.

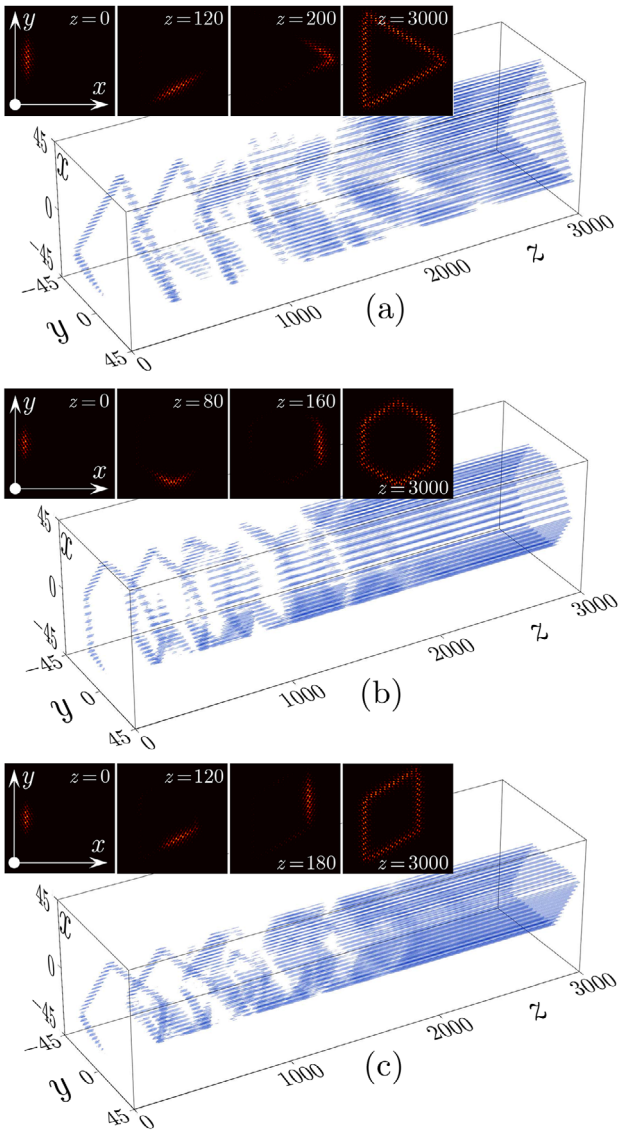

Figure 6. Examples of topological lasing patterns with moving VHESs in different geometries. Circulation of the VHESs and transition to stable lasing in a) triangular, b) hexagonal, and c) rhombic structures at $\gamma = 0.005$, $p_{\mathrm{im}} = 0.045$ and $\alpha = 0.3$. The initial state corresponds to the nonlinear edge state with momentum $k = 0.1\mathrm{K}$ with superimposed envelope of the width $w = 9b$.

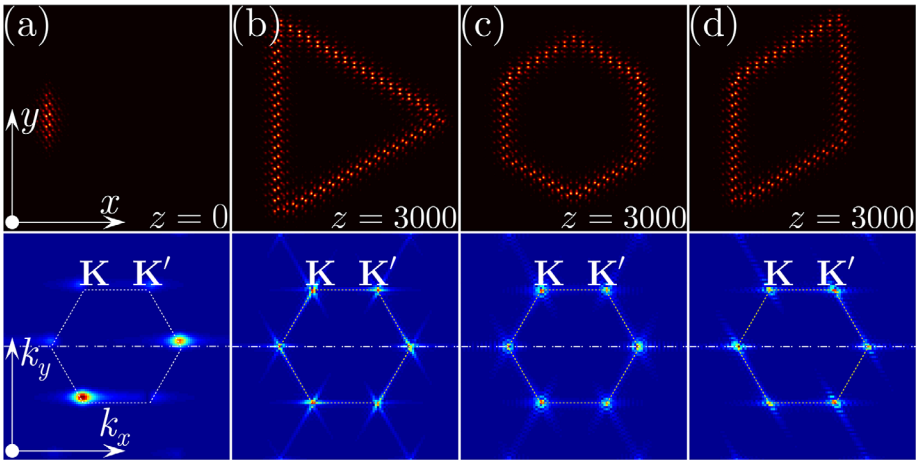

Figure 7. Amplitude distributions of the input and output states in real (first row) and momentum (second row) spaces. a) Input beam in figure corresponds to nonlinear edge state with $k = 0.1$K with a broad Gaussian envelope. b–d) Output beams in three different finite structures corresponding to Figure 6a–c. Dotted hexagons represent the first Brillouin zone, dashed line corresponds to $k_y = 0$.

we design domains of triangular, hexagonal and rhombus shapes (**Figure 5**a1–c1) with type-I gain profile in all three cases (Figure 5a2–c2).

If a moving nonlinear VHES corresponding to $k = 0.1$ K with a broad Gaussian envelope $\exp(-y^2/w^2)$ of the width $w = 9b$ is launched into such structures on their left vertical edges, one observes gradual transition from circulation of this localized state along the perimeter of the structure to lasing on the entire perimeter. This transition is illustrated with isosurfaces plots and insets showing intensity distributions at different distances in triangular (**Figure 6**a), rhombic (Figure 6b) and hexagonal (Figure 6c) finite structures. Notice that for selected parameters one observes at least two complete roundtrips of the localized initial state over the perimeter of the structure without noticeable reflections in the corners before that the amplification counterbalanced by the nonlinear absorption leads to transition to stable lasing along the entire perimeter (this typically happens at distances $z \approx 1500$). Notice that the absence of radiation in the bulk of these structures illustrate the topological regime of operation.

We would like to emphasize that because in this system time-reversal symmetry is not broken, the direction of motion of the VHES along the boundary of the structure before the onset of stable lasing along the entire perimeter is determined exclusively by the Bloch momentum of the initial state. If the VHES at $k = -0.1$ K is chosen as an input, it will move along the clockwise direction, rather than in the counterclockwise one, as in Figure 6. In **Figure 7**, we also display the input and output beams from Figure 6 in the momentum space. For the input, we use the nonlinear mode at $k = 0.1$ K with a wide Gaussian envelope, so in the momentum space, the distribution is shifted upward by 0.1 K. In addition, we found that the input excites only two **K** valleys at the Brillouin zone edge, but in the output distributions all **K** as well as **K′** valleys are excited due to inter-valley scattering after long distance propagation.

Importantly, for triangle and honeycomb finite structures the sign of the momentum of the input nonlinear state uniquely determines the direction of the output energy flow in the structure. While emerging output field modulus distributions $|\psi|$ are identical for opposite values of the initial momentum k, phase distributions are clearly distinct (topological charges of vortices emerging in the field distribution will be opposite for $+k$ and $-k$). Such a direct relation between input and output states is not found in the case of rhombic structure. Detailed information is supplied in the Supporting Information (please see Section 2 and Figure S2, Supporting Information).

4. Summary

In conclusion, we have proposed VHES lasing in inversion symmetry-breaking honeycomb lattices with gain applied to the armchair domain wall. The balance between diffraction, focusing nonlinearity, uniform loss, nonlinear absorption, and gain can allow for lasing and the formation of topologically protected nonlinear VHESs. We found that increasing gain could destabilize the lasing modes, while increasing nonlinear absorption broadens their stability intervals. Compact design of VHES lasers with different geometries has also been proposed. Such lasers do not require real or artificial magnetic fields for their operation and may inspire the investigation of topological VHESs in non-Hermitian systems.

5. Note Added in Revision

A paper[59] on electrically pumped topological lasers with valley edge modes, partially related to our work, was published after submission of this paper. Also, we became aware of another similar paper about topological lasers in valley Hall photonic crystal[60] after submission of this paper.

Supporting Information

Supporting Information is available from the Wiley Online Library or from the author.

Acknowledgements

The authors acknowledge Dr. Baile Zhang for helpful discussions. Y.Q.Z. acknowledges funding from the Guangdong Basic and Applied Basic Research Foundation (2018A0303130057). Y.V.K. acknowledges funding of

this study by RFBR and DFG according to the research project No. 18-502-12080. This research is supported by the National Key R&D Program of China (2017YFA0303800), Natural Science Foundation of China (U1537210), and the Fundamental Research Funds for the Central Universities (xzy012019038 and xzy022019076). Y.Q.Z. also acknowledges the computational resources provided by the HPC platform of Xi'an Jiaotong University. [Correction added after publication 2 July 2020: In the last sentence of the Figure 6 caption, the term "linear" was corrected to "nonlinear"]

Conflict of Interest

The authors declare no conflict of interest.

Keywords

edge state, topological insulator, topological laser, valley hall effect

Received: January 1, 2020
Revised: April 21, 2020
Published online: June 22, 2020

[1] L. Lu, J. D. Joannopoulos, M. Soljačić, *Nat. Photonics* **2014**, *8*, 821.
[2] T. Ozawa, H. M. Price, A. Amo, N. Goldman, M. Hafezi, L. Lu, M. C.Rechtsman, D. Schuster, J. Simon, O. Zilberberg, I. Carusotto, *Rev. Mod. Phys.* **2019**, *91*, 015006.
[3] M. Z. Hasan, C. L. Kane, *Rev. Mod. Phys.* **2010**, *82*, 3045.
[4] X.-L. Qi, S.-C. Zhang, *Rev. Mod. Phys.* **2011**, *83*, 1057.
[5] F. D. Haldane, S. Raghu, *Phys. Rev. Lett.* **2008**, *100*, 013904.
[6] Z. Wang, Y. Chong, J. D. Joannopoulos, M. Soljacic, *Nature* **2009**, *461*, 772.
[7] N. H. Lindner, G. Refael, V. Galitski, *Nat. Phys.* **2011**, *7*, 490.
[8] M. Hafezi, E. A. Demler, M. D. Lukin, J. M. Taylor, *Nat. Phys.* **2011**, *7*, 907.
[9] R. O. Umucalilar, I. Carusotto, *Phys. Rev. Lett.* **2012**, *108*, 206809.
[10] M. C. Rechtsman, J. M. Zeuner, Y. Plotnik, Y. Lumer, D. Podolsky, F. Dreisow, S. Nolte, M. Segev, A. Szameit, *Nature* **2013**, *496*, 196.
[11] M. Hafezi, S. Mittal, J. Fan, A. Migdall, J. Taylor, *Nat. Photonics* **2013**, *7*, 1001.
[12] A. B. Khanikaev, S. H. Mousavi, W.-K. Tse, M. Kargarian, A. H. MacDonald, G. Shvets, *Nat. Mater.* **2013**, *12*, 233.
[13] W.-J. Chen, S.-J. Jiang, X.-D. Chen, B. Zhu, L. Zhou, J.-W. Dong, C. T. Chan, *Nat. Commun.* **2014**, *5*, 5782.
[14] S. Stützer, Y. Plotnik, Y. Lumer, P. Titum, N. H. Lindner, M. Segev, M. C. Rechtsman, A. Szameit, *Nature* **2018**, *560*, 461.
[15] Y. Yang, Z. Gao, H. Xue, L. Zhang, M. He, Z. Yang, R. Singh, Y. Chong, B. Zhang, H. Chen, *Nature* **2019**, *565*, 622.
[16] E. Lustig, S. Weimann, Y. Plotnik, Y. Lumer, M. A. Bandres, A. Szameit, M. Segev, *Nature* **2019**, *567*, 356.
[17] S. Klembt, T. H. Harder, O. A. Egorov, K. Winkler, R. Ge, M. A. Bandres, M. Emmerling, L. Worschech, T. C. H. Liew, M. Segev, C. Schneider, S. Höfling, *Nature* **2018**, *562*, 552.
[18] L. H. Wu, X. Hu, *Phys. Rev. Lett.* **2015**, *114*, 223901.
[19] X. Wu, Y. Meng, J. Tian, Y. Huang, H. Xiang, D. Han, W. Wen, *Nat. Commun.* **2017**, *8*, 1304.
[20] J. Noh, S. Huang, K. P. Chen, M. C. Rechtsman, *Phys. Rev. Lett.* **2018**, *120*, 063902.
[21] H. Zhong, Y. V. Kartashov, Y. Q. Zhang, D. H. Song, Y. P. Zhang, F. L. Li, Z. Chen, *Opt. Lett.* **2019**, *44*, 3342.
[22] Y. Plotnik, M. C. Rechtsman, D. Song, M. Heinrich, J. M. Zeuner, S. Nolte, Y. Lumer, N. Malkova, J. Xu, A. Szameit, Z. Chen, M. Segev, *Nat. Mater.* **2014**, *13*, 57.
[23] D. Song, D. Leykam, J. Su, X. Liu, L. Tang, S. Liu, J. Zhao, N. K. Efremidis, J. Xu, Z. Chen, *Phys. Rev. Lett.* **2019**, *122*, 123903.
[24] Y. Sun, D. Leykam, S. Nenni, D. Song, H. Chen, Y. D. Chong, Z. Chen, *Phys. Rev. Lett.* **2018**, *121*, 033904.
[25] D. Xiao, W. Yao, Q. Niu, *Phys. Rev. Lett.* **2007**, *99*, 236809.
[26] W. Yao, D. Xiao, Q. Niu, *Phys. Rev. B* **2008**, *77*, 235406.
[27] K. F. Mak, K. L. McGill, J. Park, P. L. McEuen, *Science* **2014**, *344*, 1489.
[28] O. Bleu, G. Malpuech, D. D. Solnyshkov, *Nat. Commun.* **2018**, *9*, 3991.
[29] X.-D. Chen, F.-L. Zhao, M. Chen, J.-W. Dong, *Phys. Rev. B* **2007**, *96*, 020202.
[30] J.-W. Dong, X.-D. Chen, H. Zhu, Y. Wang, X. Zhang, *Nat. Mater.* **2017**, *16*, 298.
[31] X.-T. He, E.-T. Liang, J.-J. Yuan, H.-Y. Qiu, X.-D. Chen, F.-L. Zhao, J.-W. Dong, *Nat. Commun.* **2019**, *10*, 872.
[32] F. Deng, Y. Sun, X. Wang, R. Xue, Y. Li, H. Jiang, Y. Shi, K. Chang, H. Chen, *Opt. Express* **2014**, *22*, 23605.
[33] F. Gao, H. Xue, Z. Yang, K. Lai, Y. Yu, X. Lin, Y. Chong, G. Shvets, B. Zhang, *Nat. Phys.* **2018**, *14*, 140.
[34] L. Pilozzi, C. Conti, *Phys. Rev. B* **2016**, *93*, 195317.
[35] P. St-Jean, V. Goblot, E. Galopin, A. Lemaítre, T. Ozawa, L. Le Gratiet, I. Sagnes, J. Bloch, A. Amo, *Nat. Photonics* **2017**, *11*, 651.
[36] M. Parto, S. Wittek, H. Hodaei, G. Harari, M. A. Bandres, J. Ren, M. C.Rechtsman, M. Segev, D. N. Christodoulides, M. Khajavikhan, *Phys. Rev. Lett.* **2018**, *120*, 113901.
[37] H. Zhao, P. Miao, M. H. Teimourpour, S. Malzard, R. El-Ganainy, H.Schomerus, L. F, *Nat. Commun.* **2018**, *9*, 981.
[38] S. Longhi, Y. Kominis, V. Kovanis, *EPL* **2018**, *122*, 14004.
[39] S. Malzard, H. Schomerus, *New J. Phys.* **2018**, *20*, 063044.
[40] B. Bahari, A. Ndao, F. Vallini, A. El Amili, Y. Fainman, B. Kanté, *Science* **2017**, *358*, 636.
[41] G. Harari, M. A. Bandres, Y. Lumer, M. C. Rechtsman, Y. D. Chong, M. Khajavikhan, D. N. Christodoulides, M. Segev, *Science* **2018**, *359*, eaar4003.
[42] M. A. Bandres, S. Wittek, G. Harari, M. Parto, J. Ren, M. Segev, D. N.Christodoulides, M. Khajavikhan, *Science* **2018**, *359*, eaar4005.
[43] S. K. Ivanov, Y. Q. Zhang, Y. V. Kartashov, D. V. Skryabin, *APL Photonics* **2019**, *4*, 126101.
[44] M. Seclì, M. Capone, I. Carusotto, *Phys. Rev. Res.* **2019**, *1*, 033148.
[45] Y. V. Kartashov, D. V. Skryabin, *Phys. Rev. Lett.* **2019**, *122*, 083902.
[46] A. Drouot, M. I. Weinstein, arXiv:1910.03509, **2019**.
[47] J. Li, R.-X. Zhang, Z. Yin, J. Zhang, K. Watanabe, T. Taniguchi, C. Liu, J. Zhu, *Science* **2018**, *362*, 1149.
[48] L. Zhang, Y. Yang, M. He, H.-X. Wang, Z. Yang, E. Li, F. Gao, B. Zhang, R. Singh, J.-H. Jiang, H. Chen, *Laser Photonics Rev.* **2019**, *13*, 1900159.
[49] T. Ma, G. Shvets, *New J. Phys.* **2016**, *18*, 025012.
[50] Z. Qiao, J. Jung, Q. Niu, A. H. Macdonald, *Nano Lett.* **2011**, *11*, 3453.
[51] Z. Qiao, J. Jung, C. Lin, Y. Ren, A. H. MacDonald, Q. Niu, *Phys. Rev. Lett.* **2014**, *112*, 206601.
[52] Y. Ren, Z. Qiao, Q. Niu, *Rep. Prog. Phys.* **2016**, *79*, 066501.
[53] S. Yves, R. Fleury, T. Berthelot, M. Fink, F. Lemoult, G. Lerosey, *Nat. Commun.* **2017**, *8*, 16023.
[54] A. B. Khanikaev, G. Shvets, *Nat. Photonics* **2017**, *11*, 763.
[55] Z.-K. Shao, H.-Z. Chen, S. Wang, X.-R. Mao, Z.-Q. Yang, S.-L. Wang, X.-X. Wang, X. Hu, R.-M. Ma, *Nat. Nanotechnol.* **2020**, *15*, 67.
[56] A. Zakery, S. R. Elliott, *Optical Nonlinearities in Chalcogenide Glasses and their Applications*, Springer, Berlin **2007**.
[57] F. Smektala, C. Quemard, V. Couderc, A. Barthelemy, *J. Non Cryst. Solids* **2000**, *274*, 232.
[58] J. Harrington, *Infrared Fibers and their Applications*, SPIE Press, Bellingham, WA **2003**.
[59] Y. Zeng, U. Chattopadhyay, B. Zhu, B. Qiang, J. Li, Y. Jin, L. Li, A. G. Davies, E. H. Linfield, B. Zhang, Y. Chong, Q. J. Wang, *Nature* **2020**, *578*, 246.
[60] Y. Gong, S. Wong, A. J. Bennett, D. L. Huffaker, S. S. Oh, arXiv:2001.03661, **2020**.

